**Research Article**

# Selenium confined in ZIF-8 derived porous carbon@MWCNTs 3D networks: tailoring reaction kinetics for high performance lithium-selenium batteries

Hong-Yan Li[1,2,#], Chao Li[1,2,#], Ying-Ying Wang[1,2], Ming-Hui Sun[1,2], Wenda Dong[3], Yu Li[3,*], Bao-Lian Su[1,2,3,*]

[1]Laboratory of Inorganic Materials Chemistry (CMI), University of Namur, Namur B-5000, Belgium.
[2]Namur Institute of Structured Matter (NISM), University of Namur, Namur B-5000, Belgium.
[3]State Key Laboratory of Advanced Technology for Materials Synthesis and Processing, Wuhan University of Technology, Wuhan 430074, Hubei, China.
[#]Authors contributed equally.

*Correspondence to: Prof. Bao-Lian Su, Laboratory of Inorganic Materials Chemistry (CMI), University of Namur, Rue de Bruxelles 61, Namur B-5000, Belgium. E-mail: bao-lian.su@unamur.be/baoliansu@whut.edu.cn; Prof. Yu Li, State Key Laboratory of Advanced Technology for Materials Synthesis and Processing, Wuhan University of Technology, 122 Luoshi Road, Wuhan 430074, Hubei, China. E-mail: yu.li@whut.edu.cn

## Abstract

Lithium-selenium battery is nowadays a highly competing technology to the commercial Li-ion battery because it has a high volumetric capacity of 3253 mAh cm$^{-3}$ and gravimetric capacity of 675 mAh g$^{-1}$. However, the practical application of lithium-selenium (Li-Se) batteries is impeded by the shuttle effect of the soluble polyselenides during the cycling process. Herein, we report the in situ growth and pyrolysis of the metal-organic framework zeolitic imidazolate framework-8 (ZIF-8) on three-dimensional (3D) interconnected highly conductive multiwalled carbon nanotubes (MWCNTs). The obtained composites are used to anchor Se for advanced Li-Se batteries. Compared with the isolated ZIF-8 derived microporous carbon, our synthesized ZIF-8 derived porous carbon@MWCNTs (ZIF-8-C@MWCNTs) 3D highly conductive networks facilitate lithium ion diffusion and electron transportation. The particle size of ZIF-8 crystals has an important impact on the battery performance. By adjusting the particle size of ZIF-8, the electrochemical reaction kinetics in ZIF-8-C@MWCNTs 3D networks can be tuned. The optimized particle size of ZIF-8 around 300-500 nm coated on MWCNTs composite achieves an excellent initial

discharge capacity of 756 mAh g$^{-1}$ and a stabilized capacity of 468 mAh g$^{-1}$ at 0.2 C after 200 cycles. Combining the 3D MWCNTs with the appropriate size of ZIF-8 derived microporous carbon particles could highly improve the performance of the Li-Se battery. This work provides significant guidance for further structural design and host particle size selection for high-performance Li-Se batteries.

## INTRODUCTION

With the increase of global energy demand, the design of advanced energy materials for energy storage applications including smart power grids, commercial electronics, and electric cars has attracted considerable attention[1]. Elemental sulfur, when employed as a positive electrode material in a Li-S battery, has a high theoretical specific capacity of 1672 mAh g$^{-1}$ and a theoretical energy density of 2600 Wh kg$^{-1}$[2]. Moreover, sulfur has other advantages, such as high natural abundance, competitive cost, and minimum environmental impact[3]. Hence, it is one of the most promising positive electrode materials for next-generation energy storage systems. Although the concept of Li-S batteries has been known for years and attracts intensive research interest, several key issues in Li-S batteries, such as the shuttle effect and the inherent electric insulation property of sulfur, lead to quick capacity fading, low active-material utilization, and poor positive electrode conductivity, severely hindering their commercial application[4,5].

Selenium, another element from the same main group, has been considered as a competitive candidate, which owns a similar reaction mechanism and comparable volumetric capacity (3253 mAh cm$^{-3}$) compared with sulfur but with much improved electric conductivity ($1 \times 10^{-3}$ S m$^{-1}$)[6]. However, the shuttle effect generated by the soluble intermediates polyselenides ($Li_2Se_n$, $n \geq 4$) still exists in Li-Se batteries and leads to quick capacity decay, poor cycle performance, and low coulombic efficiency[7]. Besides, the pure selenium positive electrode is subject to volume expansion, and the lithium ion and electrical conductivity are still not efficient enough[8,9]. To address these drawbacks, the widely used effective approach is the confinement of selenium in porous carbon matrix materials. The carbon systems containing microporous, mesoporous, and even hierarchically porous structures with diverse morphologies and architectures, such as spheres[10], 1D nanotubes[11], 2D graphene[12], 3D hierarchical structures[13-15], hollow nanostructures[16], core-shell structures[17,18], *etc.*, lead to the efficiency improvement in the performance of Li-Se batteries. After the first utilization of the typical ordered mesoporous carbon CMK-3 to Li-S batteries, achieving good cycling stability with 80% of the theoretical capacity of sulfur, CMK-3 was used to confine selenium by Yang *et al.*[19] and delivered a high reversible discharge capacity[19,20].

More recently, metal-organic frameworks (MOFs) have attracted increasing attention in battery research area owing to their high surface area, uniform pore size, chemical composition, and structural diversity[21-24]. Among them, zeolitic imidazolate frameworks (ZIFs), which are based on metal imidazolates, are widely investigated because of their tunable pore sizes, apparent thermal stability, and chemical functionality. Generally, ZIF-8 can be synthesized by green, fast, and massive methods in aqueous or methanol solution, or by more environmentally friendly solid-state mechanochemistry methods at room temperature[25-27]. ZIF-8 has a pore aperture of 0.34 nm in diameter, providing the possibility to adsorb small gas molecules and store the adsorbed materials in the cavity (1.11 nm). Zhou *et al.*[28] first used ZIF-8 nanocrystals as the host with 30 wt.% sulfur loading, achieving long cycle capabilities in a Li-S battery. They further proved that the particle size of MOF significantly influences the final battery performance, because hosts mainly affect the internal Li$^+$/e$^-$ transport. However, the poor conductivity of MOFs leads to low capacity and rate capability, so it is ineffective to directly confine selenium inside the pores with a high amount. The pyrolysis of ZIF-8

can precisely maintain the particle size, morphology, and structure, but with much improved conductivity, which has recently attracted much attention[29-33]. Zheng *et al.*[11] reported nitrogen-doped graphene particle analogs with a high nitrogen content from the pyrolysis of a nitrogen-containing zeolitic imidazolate framework as lithium anode materials. This idea was further extended to sodium anode batteries[17]. The ZIF-8 derived high-level N-doped graphene analogous particles obtained by pyrolysis as an anode material exhibited excellent electrochemical performance for lithium and sodium batteries. The porous carbon host from ZIF-8 pyrolysis used for lithium-selenium batteries by Liu *et al.*[34] showed that the interconnected microporous carbon polyhedrons (1.1 nm) would have a large surface area and pore volume to effectively confine Se and withstand volume variation. Besides, the dissolution of polyselenides in electrolytes would be suppressed at the same time. Li *et al.*[35] used $NH_3$ to enlarge the microporous structure to create a hierarchically mesoporous structure. The obtained sulfur- and ZIF-8 derived porous carbon composites resulted in twice higher capacity retention than that of MOF-C made by direct pyrolysis of MOFs. However, the conductivity of MOF-derived porous carbon is still not high enough due to relatively low graphitic crystallinity, together with the aggregation, which will lead to sluggish lithium ion transport and insufficient contact with dissolved polyselenides[36-38]. In addition, the poor flexibility of microporous carbon materials derived from the pyrolysis of MOFs limits its future application in highly efficient flexible electronic devices. Carbon nanotubes (CNTs) have been widely applied in the energy area because of their one-dimensional electronic conductivity, great surface area, and mechanical properties[39]. It is possible to build fast three-dimensional electron transportation pathways with multiwalled CNTs (MWCNTs) entanglement[40]. ZIF decorated on MWCNT-derived materials has proven to be a feasible approach to achieving high-efficiency supercapacitors[41] and can be used as anode materials[42,43]. The 3D MIL-68 (Al)@MWCNTs obtained by in situ pyrolyzing MIL-68 particles on the surface of MWCNTs have recently been reported to achieve excellent performance in a Li-Se battery[44].

Herein, we report 3D structured microporous carbon/MWCNT composite materials for selenium confinement through in situ formations of ZIF-8-coated MWCNTs by feasible solvothermal reaction and their pyrolysis for lithium-selenium batteries. Such ZIF-8 derived porous carbon@MWCNTs 3D networks can effectively accelerate electrons transport, provide the pathways for $Li^+$ transfer, and enhance the adsorption of the polyselenides, which will further improve the reaction kinetics. The ZIF-8 derived microporous carbon particle sizes are tuned from 30 nm to 1.5 μm with a modulator. The rich micropores serve the sites for Se loading and possess strong adsorption to polyselenides. The pyrolyzed ZIF-8 with particle size around 300 nm-500 nm coated on MWCNT composites retained the best specific capacity of 468 mAh $g^{-1}$ at 0.2 C after 200 cycles. The unique 3D structure with the tunable size of pyrolyzed ZIF-8 particles can confine the soluble polyselenides, accelerate $Li^+$ transfer, promote the conductivity of positive electrode materials, and optimize the electrochemical reaction kinetics, thereby leading to an excellent electrochemical property. This work reveals enormous advantages for the MWCNTs in tandem with the tunable ZIF-8 derived microporous carbon particles and explores their optimal combination. The achieved outstanding property is one step closer to having a potential commercial application of the Li-Se battery.

## EXPERIMENTAL
### Preparation of ZIF-8
Typically, a solution of $Zn(NO_3)_2 \cdot 6H_2O$ (470 mg) in 50 mL of methanol was rapidly poured into a solution of 2-methylimidazole (Hmim, 810 mg) in 50 mL of methanol under stirring. The mixture slowly turned turbid after 30 min, and then was kept stirring for another 2 h. Finally, the white ZIF-8 nanocrystals were separated from the milky dispersion by centrifugation and washing with fresh methanol three times. The nanocrystals were dried at 40 °C in vacuum. It is worth noting that the dried ZIF-8 will not be redispersible in methanol again.

**Preparation of ZIF-8@MWCNTs**

Before synthesis, MWCNTs were pretreated with strong acid to decorate oxygen-containing functional groups at the surface to facilitate the growth of ZIF-8 crystals on the surface of MWCNTs. Then, 30 mg of modified MWCNTs were added into the solution of Hmim (810 mg) in 50 mL of methanol with strong ultrasound, following the exact same procedure as for ZIF-8. Finally, a grey black powder was obtained compared to the white crystals of ZIF-8. The obtained composite was denoted as ZIF-8@MWCNTs-1. Different weight percentages of 1-methylimidazole as a modulator, namely 50 wt.%, 70 wt.%, 90 wt.%, and 100 wt.%, compared to the weight of ligand 2-methylimidazole were added to give ZIF-8@MWCNTs-2, ZIF-8@MWCNTs-3, ZIF-8@MWCNTs-4, and ZIF-8@MWCNTs-5, respectively.

**Preparation of ZIF-8 derived porous carbon (ZIF-8-C) and ZIF-8 derived porous carbon coated MWCNTs (ZIF-8-C@MWCNTs)**

The as-synthesized ZIF-8 and ZIF-8@MWCNTs-X (X = 1-5) were calcined at 800 °C with a heating rate of 5 °C min$^{-1}$ for 4 h in an argon atmosphere. To completely remove the zinc species, the acquired black powder was immersed in 4 M HCl aqueous solution at room temperature for 12 h. After washing three times with deionized water to pH equal to 7, the products dried in a vacuum oven overnight were labeled as ZIF-8-C, ZIF-8-C@MWCNTs-1, ZIF-8-C@MWCNTs-2, ZIF-8-C@MWCNTs-3, ZIF-8-C@MWCNTs-4, and ZIF-8-C@MWCNTs-5, respectively.

**Se confinement in ZIF-8-C and ZIF-8-C@MWCNTs-X (X = 1-5)**

The selenium confined porous carbon composites were synthesized by two-step melt-diffusion procedures. With a weight ratio of 2:1, bulk Se (Sigma-Aldrich) and ZIF-8-C or ZIF-8-C@MWCNTs-X (X = 1-5) materials were then thoroughly mixed by ball milling. The mixtures were heated up to 260 °C and maintained for 16 h in a tube furnace full of flowing Ar, followed by 300 °C for 2 h to obtain the composites. The final products were labeled as Se@ZIF-8-C, Se@ZIF-8-C@MWCNTs-1, Se@ZIF-8-C@MWCNTs-2, Se@ZIF-8-C@MWCNTs-3, Se@ZIF-8-C@MWCNTs-4, and Se@ZIF-8-C@MWCNTs-5, respectively.

**Materials characterization**

X-ray diffraction (XRD) patterns were obtained on a Bruker D8 system with Cu Kα radiation (λ = 0.15405 nm) at 40 mA and 30 kV. Scanning electron microscopy (SEM) observation was carried out using a JEOL 7500 F field-emission SEM. Transmission electron microscopy (TEM) images of the samples were recorded on carbon-coated copper grids by using a TECNAI 10 at an acceleration voltage of 100 kV. Nitrogen adsorption-desorption isotherms were obtained using an ASAP 2420 surface area and porosity analyzer at 77 K. The specific surface area was calculated by the Brunauer-Emmett-Teller (BET) method. The pore size distribution was calculated using the Barrett-Joyner-Halenda (BJH) method for mesopores and nonlocal density functional theory (NLDFT) for the micropores analysis method. Thermogravimetric analysis (TGA) was carried out using a thermal analyzer (Setaram Labsys Evo) under a flow of nitrogen with a temperature ramp of 5 °C min$^{-1}$. X-ray photoelectron spectroscopy (XPS) characterization was carried out in a ThermoFisher ESCALAB 250 Xi instrument with a monochromatic Al Kα X-ray source (1486.6 eV).

**Electrochemical measurements**

The electrochemical measurements were carried out at room temperature using CR2032 coin-type cells. The working electrode was prepared by mixing with active material, Super-P carbon (Timcal), and sodium alginate (SA, Sigma-Aldrich) at the weight ratio of 8:1:1 in distilled water. The resulting slurry was coated onto aluminum foil and dried in vacuum at 60 °C overnight. The coin-type cells were assembled in an Ar-filled glovebox with moisture and oxygen concentrations lower than 1 ppm, using lithium metal as the counter/reference electrode, glass fiber membrane as the separator, and 1 M lithium bis(trifluoromethanesulfonyl)imide (LiTFSI) (Solvay) in a mixture of dioxolane (DOL, Sigma-Aldrich), and dimethoxygethane (DME, Sigma-Aldrich) (1:1 in volume) with 1% $LiNO_3$ (Sigma-Aldrich) additive as the

electrolyte. The galvanostatic discharge and charge experiments were performed on a battery tester (LAND) with a voltage window of 1.75 V-2.6 V *vs.* Li+/Li at different current densities of 0.1 C, 0.2 C, 0.5 C, 1 C, 2 C, and 5 C (1 C = 675 mA g$^{-1}$). Cyclic voltammetry (CV) was performed using an electrochemical workstation Princeton VersaSTAT 3 at a voltage of 1.75 V -2.6 V with a scan rate of 0.1 mV s$^{-1}$. Electrochemical impedance spectroscopy (EIS) measurement was also conducted using Princeton VersaSTAT 3 with a frequency range between 100 kHz and 10 mHz.

## RESULTS AND DISCUSSION

Compared to the preparation of ZIF-8@MWCNTs by two-step method including filtering the metal salts with MWCNTs followed by adding of 2-methylimidazole (Hmim) reported in the literature[45,46], our novel method is notably much simpler, but it can also tune the ZIF-8 crystal size grown on MWCNTs. Figure 1A and B schematically illustrates the preparation process of Se@ZIF-8-C@MWCNTs and the tunable crystal sizes of the ZIF-8 in the ZIF-8-C@MWCNTs 3D network composites. Our present work demonstrates that ZIF-8 with variable crystal sizes can directly grow on the surface of MWCNTs via a simple mixing reaction in methanol at room temperature. The ZIF-8 as a reference sample was synthesized by simple mixing of zinc salts and 2-methylimidazole in the methanol at room temperature. The ZIF-8@MWCNTs composites were synthesized by in situ growth of ZIF-8 crystals on oxidized MWCNTs with the different weight ratio of modulator (1-methylimidazole). The modulator was used to tune the size of ZIF-8 crystals. The higher the amount of modulator, the larger the crystal size. ZIF-8 with different crystal sizes grown on MWCNTs were obtained [Figure 1B]. When the ZIF-8 crystal size is small, it grows along the single nanotube where only one nanotube is across the ZIF-8 crystal. As the crystal size increases, multiple CNTs pass through the ZIF-8 crystals. The ZIF-8 derived porous carbons (ZIF-8-C) and ZIF-8 derived porous carbon on 3D multiwalled carbon nanotubes (ZIF-8-C@MWCNTs) were obtained by the pyrolysis of ZIF-8 crystals at 800 °C in argon, followed by acid washing to remove the metal. Finally, the selenium was confined inside the pores of the composites at 260 °C [Figure 1C].

The successful synthesis of ZIF-8@MWCNTs was confirmed by X-ray powder diffraction [Figure 2A]. The two broad peaks at 26° and 43.5° (2θ) in the XRD pattern of MWCNTs correspond to the (002) and (100) Bragg reflection planes with low crystallinity[47]. In terms of ZIF-8, the diffraction peaks at 7.3°, 10.3°, 12.7°, and 18° (2θ), representing the crystal structures of ZIF-8 are observed, being consistent with its typical crystalline structure (CCDC # 602542)[48,49]. After the addition of MWCNTs, the peaks of ZIF-8 appear at the same positions, which proved the successful synthesis of the ZIF-8@MWCNTs composites. Due to the high intensity of the ZIF-8, the broad peaks belonging to MWCNTs are indistinguishable. Supplementary Figure 1 demonstrates that there is no effect on the formation of ZIF-8 crystalline structure by adding MWCNTs in the synthesis, and that the peak intensity of ZIF-8@MWCNTs composite increases with increasing the amount of modulator (1-methylimidazole) as the crystal size of ZIF-8 in situ grown on MWCNTs gradually increased. Following the high-temperature pyrolysis at 800 °C, the 3D network composites made of ZIF-8 derived porous carbon and MWCNTs were obtained. The XRD pattern of ZIF-8-C indicates the carbon derived from ZIF-8 is in an amorphous state. After the encapsulation of selenium in ZIF-8-C@MWCNTs composites, the characteristic peaks of selenium at 23.5° and 29.5° (2θ) almost disappear from Se@ZIF-8-C@MWCNTs-1 as a representative sample, indicating that the selenium is in the amorphous phase[50].

The confinement condition of selenium inside ZIF-8-C@MWCNTs-X (X = 1-5) composites can also be confirmed by the N$_2$ adsorption-desorption isotherms [Figure 2B and Supplementary Figure 2]. The adsorption-desorption isotherms of ZIF-8-C and the ZIF-8-C@MWCNTs-X (X = 1-5) composites display typical Type I curves with hysteresis at a high relative pressure of 0.8-1.0, showing the microporous characteristics with the presence of interparticular large pore size of these materials. The pore size
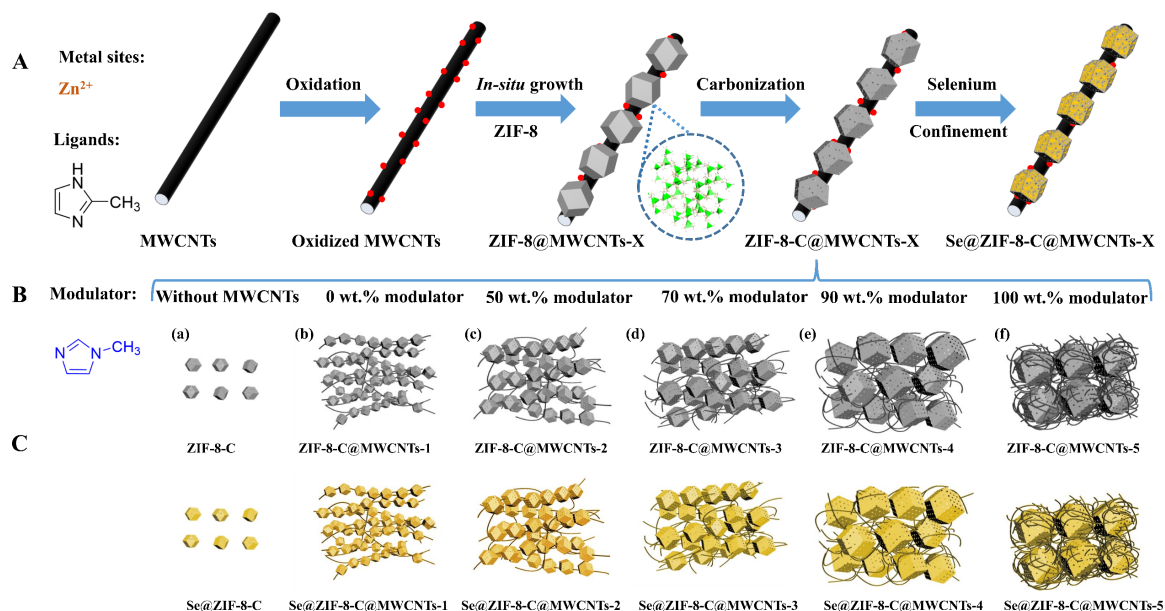
**Figure 1.** (A) Schematic synthesis routes of ZIF-8-C@MWCNTs-X, (B) tuning of the size of ZIF-8 for a series of ZIF-8-C@MWCNTs-X (X = 1-5) and (C) synthesis the final selenium-confined composites of Se@ZIF-8-C, Se@ZIF-8-C@MWCNTs-1, Se@ZIF-8-C@MWCNTs-2, Se@ZIF-8-C@MWCNTs-3, Se@ZIF-8-C@MWCNTs-4, and Se@ZIF-8-C@MWCNTs-5, respectively.
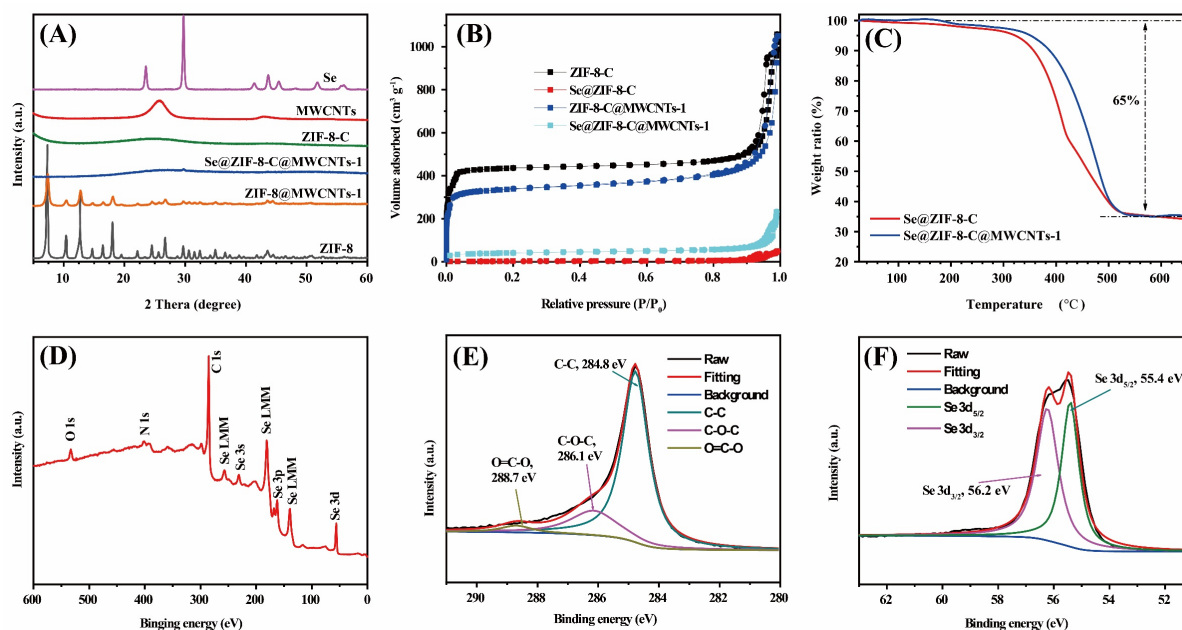


**Figure 2.** (A) XRD patterns of ZIF-8, MWCNTs, ZIF-8@MWCNTs-1, ZIF-8-C, Se@ZIF-8-C@MWCNTs-1, and selenium. (B) Nitrogen adsorption and desorption isotherms of ZIF-8-C, Se@ZIF-8-C, ZIF-8-C@MWCNTs-1 and Se@ZIF-8-C@MWCNTs-1. (C) TGA curves of Se@ZIF-8-C and Se@ZIF-8-C@MWCNTs-1 under nitrogen with a rate of 5 °C min$^{-1}$. XPS spectrum of Se@ZIF-8-C@MWCNTs-1: (D) Survey scan; (E) C1s; and (F) Se3d.

distribution curves show the presence of two kinds of micropores, 1.0 nm and 1.5 nm, in all the as-prepared materials [Supplementary Figure 2]. The hysteresis at the very high relative pressure over 0.8 [Supplementary Figure 2A and B] is due to the intergranular porosity coming from the aggregation of ZIF-8

derived porous carbon particles. The calculated BET surface areas and pore volumes are listed in Supplementary Table 1. The pore volume and surface area decrease with increasing the amount of modulator, and then increase back to 1.32 cm³ g⁻¹ and 1283 m² g⁻¹, respectively. After selenium loading, the micropores disappear, indicating that the pores were filled with selenium [Figure 2B].

The exact weight ratio of selenium in Se@ZIF-8-C and Se@ZIF-8-C@MWCNTs-X (X = 1-5) composites were measured by TGA. The TG curves of Se@ZIF-8-C and Se@ZIF-8-C@MWCNTs-1 as representative samples are shown in Figure 2C. The series of Se@ZIF-8-C@MWCNTs-X are given in Supplementary Figure 3. In Figure 2C, a weight loss is observed at around 200 °C, because of the small amount of selenium residue at the surface of ZIF-8-C@MWCNTs-1. The main weight loss starts from 300 °C to 500 °C, which is responsible for the encapsulated selenium. The selenium weight ratio of Se@ZIF-8-C and Se@ZIF-8-C@MWCNTs-X (X = 1-5) are around 65%. The high Se loading proportion in the Se@host composites is due to the high surface area and high pore volume of all the host materials. XPS was also applied to investigate the elemental composition and ratio and the electronic state of the specific elements. The survey scan of the Se@ZIF-8-C@MWCNTs-1 [Figure 2D] gives the peaks located at 533, 402.6, 284 and 55.3 eV corresponding to O1s, N1s, C1s, and Se3d, respectively. The existence of O1s peak with very low intensity may be due to the physically adsorbed moisture/oxygen[51]. The peak of N1s is originally from the ligands of 2-methylimidazole. The weight ratio of selenium from the survey scan is 63.5%, which is consistent with the data from TGA. The peak of high-resolution C1s spectrum could be deconvoluted into three components at 284.8 eV, 286.1 eV, and 288.7 eV, related to C-C, C-O, and C=O, respectively [Figure 2E]. The high-resolution Se3d spectrum in Figure 2F can be deconvoluted into two contributions of 55.4 and 56.2 eV, corresponding to Se3d$_{5/2}$ and Se3d$_{3/2}$, respectively, due to spin-orbit coupling[52].

The morphologies of ZIF-8-C and ZIF-8-C@MWCNTs-X (X = 1-5) were examined by TEM and SEM, as shown in Figures 3 and 4, respectively. The particle sizes of pure ZIF-8-C are quite uniform, around 50 nm ± 10 nm. After adding oxidized MWCNTs into the methanol solution, the ZIF-8 particles clearly grew along the surface of MWCNTs, and the ZIF-8 crystal size was largely reduced to around 20 nm-30 nm. This indicates that the surface functionalization of MWCNTs by strong acid treatment favors the interaction between ZIF-8 crystals and MWCNTs, leading to the growth of ZIF-8 crystals at the surface of MWCNTs. It is interesting to note that almost all the ZIF-8 crystals grew along the MWCNTs. Increasing the amount of 1-methylimidazole as a modulator, the crystal size of ZIF-8 starts to increase. The interconnected CNT network and the ZIF-8 crystals on its surface form a sponge structure with a large number of pores inside. After the pyrolysis process, the particle sizes are 50 nm for ZIF-8-C [Figure 3A and D], 20nm-30 nm for ZIF-8-C@MWCNTs-1 [Figure 3B and E], 100 nm-150 nm for ZIF-8-C@MWCNTs-2 [Figure 3C and F], 300 nm-500 nm for ZIF-8-C@MWCNTs-3 [Figure 3G and J], 500 nm-800 nm for ZIF-8-C@MWCNTs-4 [Figure 3H and K], and 800 nm to 1.5 μm for ZIF-8-C@MWCNTs-5 [Figure 3I and L]. It clearly shows that the ZIF-8-C particles are embedded in multiple CNTs networks. Figure 4 further proves the presence of ZIF-8-C with very homogenous particle size in ZIF-8-C@MWCNTs-X (X = 1-5) composites. The SEM and TEM images of Se@ZIF-8-C are shown in Supplementary Figure 4. After confining Se into ZIF-8-C, the morphology of the obtained Se@ZIF-8-C remains unchanged. The uniform dispersion of carbon, selenium, and nitrogen was confirmed by energy-dispersive X-ray spectroscopy (EDX) element analysis mapping. The accurate weight loading of selenium inside ZIF-8-C@MWCNTs-1 is 64 wt.% by EDX element analysis, which is in agreement with the data from XPS and TGA. The other EDX mapping data of other composites are shown in Supplementary Figure 5, indicating that the C, Se, and N elements are well dispersed[53].

Coin cells were assembled with lithium metal as anode and mixtures of Se@ZIF-8-C or Se@ZIF-8-C@MWCNTs-X, conductive carbon, and sodium alginate with a weight ratio of 8:1:1 as a positive electrode
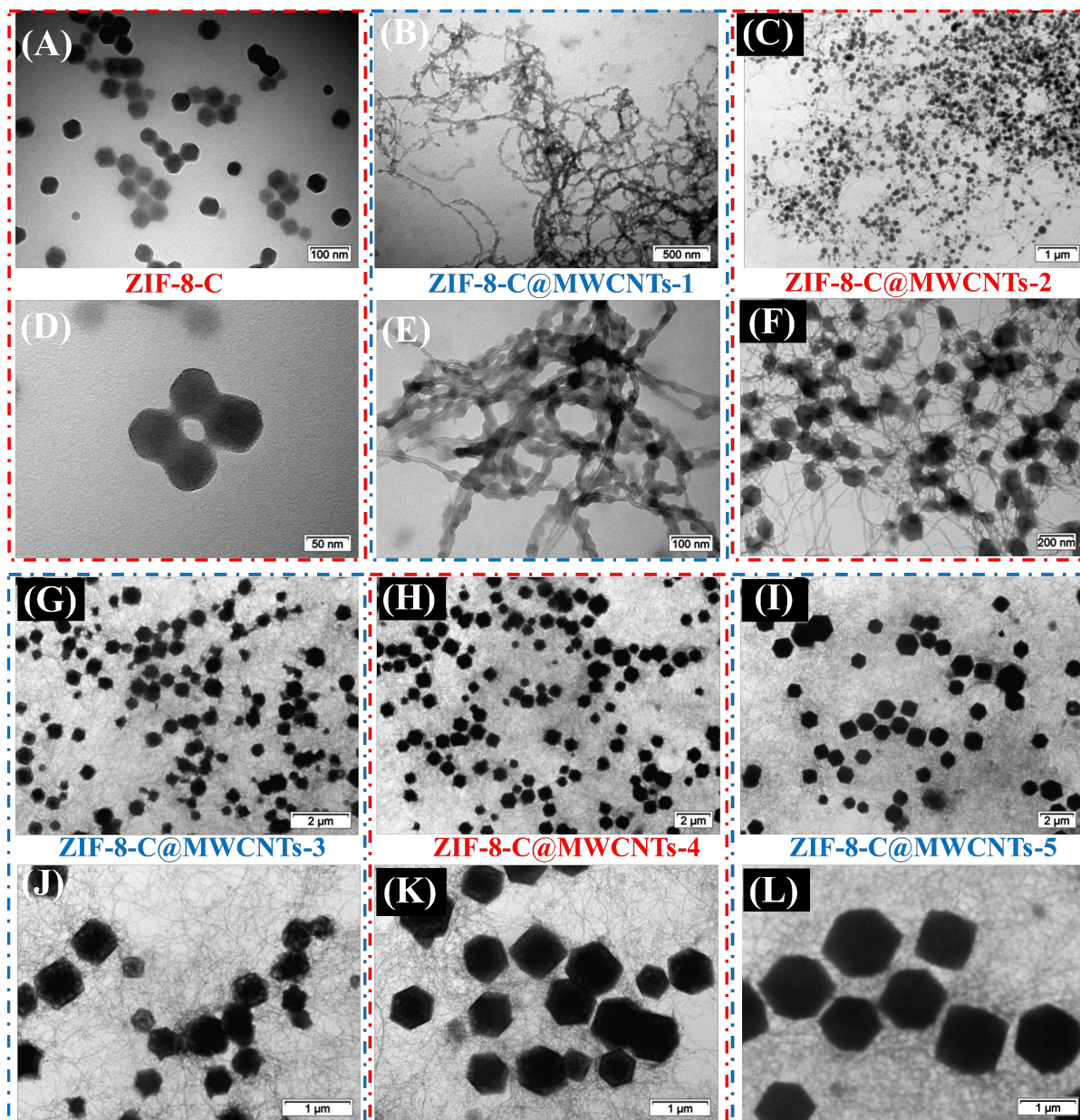
**Figure 3.** TEM images of: ZIF-8-C (A,D); ZIF-8-C@MWCNTs-1 (B,E); ZIF-8-C@MWCNTs-2 (C,F); ZIF-8-C@MWCNTs-3 (G,J); ZIF-8-C@MWCNTs-4 (H,K); and ZIF-8-C@MWCNTs-5 (I,L).

to evaluate the battery performance. The electrolyte was composed of 1 M LiTFSI DOL: DME with a volume ratio of 1:1, accompanied with 1% $LiNO_3$. From 50 to 80 μL of electrolyte were added to every cell, and glass fiber was used as the separator in our case. The typical battery voltage used was in the range of 1.75 V-2.6 V to avoid excessive $LiNO_3$ decomposition for sustainable protection as $LiNO_3$ can react with metallic lithium anode to form a passivation layer on lithium anode, at the same time getting a higher coulombic efficiency. To explore the electrochemical reaction during the discharge-charge process, CV analyses of Se@ZIF-8-C@MWCNTs-3, as representative samples of Se@ZIF-8-C@MWCNTs-X, are presented in Figure 5A. The CV curve shows two obvious reduction peaks at 2.14 V and 1.93 V at the first cycle, relevant to the stepwise electrochemical reaction from selenium to lithium polyselenides ($Li_2Se_n$, $n \geq$
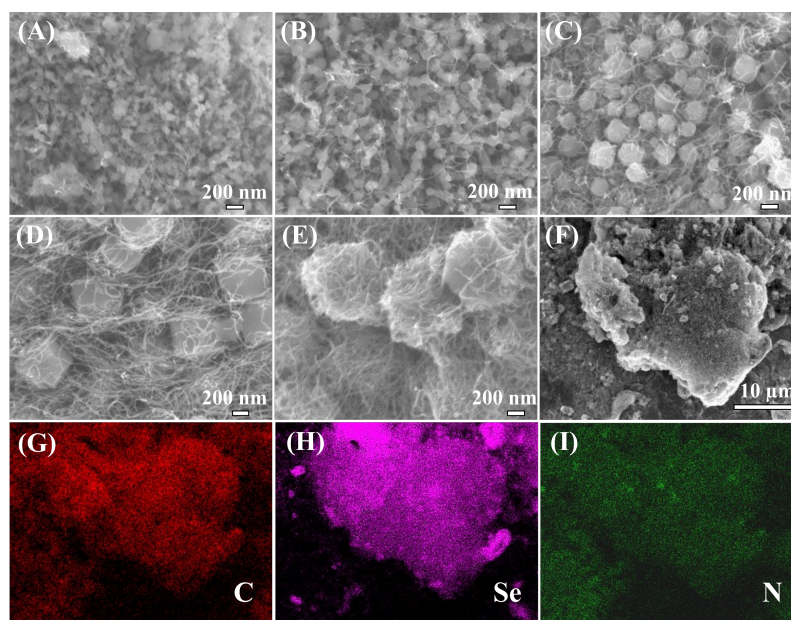
**Figure 4.** SEM images of: (A) ZIF-8-C@MWCNTs-1; (B) ZIF-8-C@MWCNTs-2; (C) ZIF-8-C@MWCNTs-3; (D) ZIF-8-C@MWCNTs-4; (E) ZIF-8-C@MWCNTs-5; and (F) Se@ZIF-8-C@MWCNTs-1. EDX mapping images of Se@ZIF-8-C@MWCNTs-1: (G) C; (H) Se; and (I) N.

4), finally to $Li_2Se$[54,55]. There is another small reduction peak observed at 2.26 V, which is due to the irreversible transformation of cyclic $Se_8$ into higher-order linear $Se_n$[51]. Two oxidation peaks corresponding to the reaction from $Li_2Se$ to Se with the intermediate $Li_2Se_n$ appear at 2.17 and 2.26 V, respectively. The following cycles show similar peaks to the first cycle, but the reduction/oxidation peaks shift to a lower overpotential position due to the formation of the solid electrolyte interphase (SEI) layer on the surface of positive electrode and the activation of Se electrode[56]. Moreover, the absence of a small reduction peak at 2.26 V in the following cycles is due to the irreversible transformation of cyclic $Se_8$ into higher-order linear $Se_n$. After that, the CV curves overlap well, demonstrating the improvement of the reversibility with cycling.

The cycling performance of Se@ZIF-8-C, Se@ZIF-8-C@MWCNTs-1, and Se@ZIF-8-C@MWCNTs-3 were carried out at 0.2 C (1 C = 675 mA $g^{-1}$) [Figure 5B]. The initial discharge/charge capacities of Se@ZIF-8-C and Se@ZIF-8-C@MWCNTs-1 are 294/613 and 422/578 mAh $g^{-1}$, respectively. The initial coulombic efficiencies of Se@ZIF-8-C and Se@ZIF-8-C@MWCNTs-1 are 48% and 76%, respectively. The low coulombic efficiencies can be attributed to the irreversible formation process of SEI in the first cycle and electrolyte decomposition[57]. After the first few cycles, the coulombic efficiencies of Se@ZIF-8-C@MWCNTs-1 quickly climbed to more than 95% and stabilized. However, Se@ZIF-8-C electrodes needed more cycles to be stabilized because of their sluggish utilization of selenium by inefficient ionic and electron mobility. After 200 cycles, the capacity of Se@ZIF-8-C@MWCNTs-1 electrode is stabilized at 216 mAh $g^{-1}$, while the capacity of Se@ZIF-8-C is sharply reduced to 150 mAh $g^{-1}$. This reflects that the electrochemical reaction was accelerated by introducing interconnected MWCNTs to the system. By optimizing the composition of MWCNTs and ZIF-8-C particles, the battery can achieve further improved performance. As shown in Figure 5B, Se@ZIF-8-C@MWCNTs-3 exhibits a high initial capacity of 756 mAh $g^{-1}$ and remains at 468 mAh $g^{-1}$ after 200 cycles. The detailed discharge/charge curves of the Se@ZIF-8-C@MWCNTs-3 electrode at the 1st, 50th, 100th, 150th, and 200th cycles are shown in Figure 5C. The discharge curves show two typical platforms, which are consistent with the cyclic voltammetry measurements containing two reduction peaks.
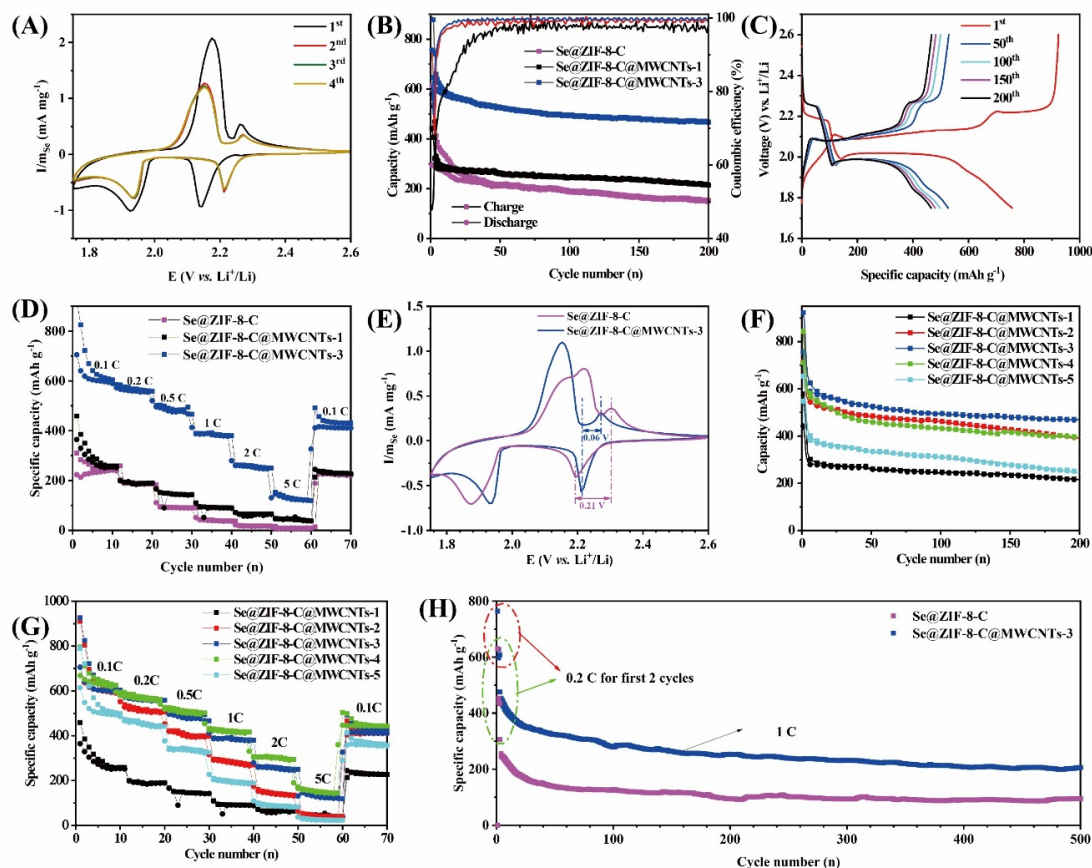
**Figure 5.** (A) Se mass-normalized CV curves of Se@ZIF-8-C@MWCNTs-3 at first four cycles. (B) The cycling performance and corresponding coulombic efficiency of Se@ZIF-8-C, Se@ZIF-8-C@MWCNTs-1, and Se@ZIF-8-C@MWCNTs-3. (C) The charge and discharge curves at different cycles of Se@ZIF-8-C@MWCNTs-3. (D) Rate capability of Se@ZIF-8-C, Se@ZIF-8-C@MWCNTs-1, and Se@ZIF-8-C@MWCNTs-3. (E) CV curves of Se@ZIF-8-C and Se@ZIF-8-C@MWCNT-3 in the fourth cycle. (F) The cycling performance and (G) rate capability of Se @ZIF-8-C@MWCNTs-1, Se@ZIF-8-C@MWCNTs-2, Se@ZIF-8-C@MWCNTs-3, Se@ZIF-8-C@MWCNTs-4, and Se@ZIF-8-C@MWCNTs-5. (H) Cycling performance of Se@ZIF-8-C and Se@ZIF-8-C@MWCNTs-3 at a high current density of 1 C.

Figure 5D shows the rate performance of Se@ZIF-8-C, Se@ZIF-8-C@MWCNTs-1, and Se@ZIF-8-C@MWCNTs-3 at current densities of 0.1, 0.2, 0.5, 1, 2, and 5 C. The capacity decreased with the increase of current densities due to the electrolyte polarization and the limitation of the ions transfer and transformation. The capacities of Se@ZIF-8-C@MWCNTs-1 are around 250, 192, 150, 100, 60 and 45 mAh g$^{-1}$ at the current densities of 0.1, 0.2, 0.5, 1, 2, and 5 C, respectively. When back to 0.1 C, a capacity of 220 mAh g$^{-1}$ is observed, showing excellent capacity recovery, indicating the stable structure of Se@ZIF-8-C@MWCNTs in high current density cycling. The rate performance of their counterpart Se@ZIF-8-C showed lower rate capacities of 220, 180, 100, 40, 20 and 10 mAh g$^{-1}$ at the current densities of 0.1, 0.2, 0.5, 1, 2, and 5 C, respectively. Se@ZIF-8-C@MWCNTs-3 present an improved capacity at different current densities than those of Se@ZIF-8-C@MWCNTs-1 and Se@ZIF-8-C, showing its superior performance. The improved performance of Se@ZIF-8-C@MWCNTs compared to Se@ZIF-8-C confirms the ability of the 3D composite with microporous carbon and interconnected CNTs networks. The encapsulation of selenium inside the porous carbon of ZIF-8-C possesses more reaction sites, and the presence of MWCNTs is beneficial to fast electron mobility, which facilitates the electrochemical kinetics of selenium species. Moreover, the 3D structure further firmly fixes the ZIF-8 in the specific position, proves the interconnected

pathways for Li$^+$ transfer, and enhances the adsorption of the polyselenides by its surface polar bonds. The CV measurements for comparison of Se@ZIF-8-C and Se@ZIF-8-C@MWCNTs-3 were performed under the same operating conditions as the battery with a voltage of 1.75-2.6 V. The CV curves of Se@ZIF-8-C and Se@ZIF-8-C@MWCNTs-3 at the fourth cycle are shown in Figure 5E. The higher current density and lower overpotential of Se@ZIF-8-C@MWCNTs-3 (0.06 V) than that of Se@ZIF-8-C (0.21 V) indicate that Se@ZIF-8-C@MWCNTs achieves accelerated electrochemical kinetics.

To explore the optimal combination of ZIF-8 derived porous carbon particles and MWCNTs, cells with a series of Se@ZIF-8-C@MWCNTs-X (X = 1-5) positive electrodes were assembled and further tested. As shown in Figure 5F, the batteries exhibit very high initial discharge capacities of 715, 756, 710, and 547 mAh g$^{-1}$ for Se@ZIF-8-C@MWCNTs-2, Se@ZIF-8-C@MWCNTs-3, Se@ZIF-8-C@MWCNTs-4, and Se@ZIF-8-C@MWCNTs-5, respectively. The higher value than the theoretical one (675 mAh g$^{-1}$) is due to the additional capacity contribution from the formation of SEI layer. The Se@ZIF-8-C@MWCNTs-X (X = 2-5) positive electrodes achieve much better performance than that of Se@ZIF-8-C@MWCNTs-1 and have a trend of increase first and then decrease with the increase of the particle size of the ZIF-8 derived porous carbons. At a ZIF-8 derived porous carbon particle size of 300 nm-500 nm, the Se@ZIF-8-C@MWCNTs-3 positive electrode reaches the best electrochemical performance. With the cycles running, the Se@ZIF-8-C@MWCNTs-2, Se@ZIF-8-C@MWCNTs-4, and Se@ZIF-8-C@MWCNTs-5 have relatively faster decay than Se@ZIF-8-C@MWCNTs-3 and stabilize at 392, 396, and 246 mAh g$^{-1}$ after 200 cycles, respectively. The capacity performance results of all the different fabricated positive electrodes are summarized in Table 1. Se@ZIF-8-C@MWCNTs-3, with the highest discharge of 468 mAh g$^{-1}$ after 200 cycles, shows the best cycling performance. This can be attributed to the appropriate particle size of ZIF-8 derived microporous carbon, ensuring the full utilization of Se and adsorption of polyselenides. To confirm the capacity contributed by Se rather than MWCNTs, the CV measurement and cycle capacity of pure-MWCNTs were conducted at 1.75 V-2.6 V. The results are shown in Supplementary Figure 6. A reduction peak at the voltage of 1.82 V is shown in Supplementary Figure 6A, which is due to the decomposition of electrolyte at low voltage and SEI layer formation during the first cycle. After that, the formed SEI separates the electrolyte and MWCNTs host material and the decomposition of electrolyte is greatly decreased. In Supplementary Figure 6B, the discharge capacity of cells with pure-MWCNTs is 156 mAh g$^{-1}$ at the first cycle, which rapidly drops to 26.7 mAh g$^{-1}$ and stabilizes at 8 mAh g$^{-1}$. This indicates that the capacity achievement in the battery with Se@ZIF-8-C@MWCNTs is contributed by active Se after the first cycle.

The rate performance of Se@ZIF-8-C@MWCNTs-X (X = 1-5) was tested at different current densities [Figure 5G], as listed in Table 2. The Se@ZIF-8-C@MWCNTs-2 exhibits the capacity of 600 mAh g$^{-1}$, 520 mAh g$^{-1}$, 405 mAh g$^{-1}$, 285 mAh g$^{-1}$, 143 mAh g$^{-1}$, and 50 mAh g$^{-1}$ at the current densities of 0.1 C, 0.2 C, 0.5 C, 1 C, 2 C, and 5 C, respectively, showing a largely improved performance compared with that of Se@ZIF-8-C@MWCNTs-1. As the size of ZIF-8 derived porous carbon increases, the capacity of Se@ZIF-8-C@MWCNTs-3 (675 mAh g$^{-1}$, 584 mAh g$^{-1}$, 496 mAh g$^{-1}$, 391 mAh g$^{-1}$, 260 mAh g$^{-1}$, and 145 mAh g$^{-1}$) and Se@ZIF-8-C@MWCNTs-4 (660 mAh g$^{-1}$, 582 mAh g$^{-1}$, 517 mAh g$^{-1}$, 426 mAh g$^{-1}$, 306 mAh g$^{-1}$, and 156 mAh g$^{-1}$) have further significant improvement at current densities of 0.1 C-5 C with high recoverability. The rate performance of Se@ZIF-8-C@MWCNTs-4 shows the same best performance as Se@ZIF-8-C@MWCNTs-3, whereas Se@ZIF-8-C@MWCNTs-5, with the largest ZIF-8 derived porous carbon particles, has a relatively reduced capacity of 564 mAh g$^{-1}$, 467 mAh g$^{-1}$, 343 mAh g$^{-1}$, 205 mAh g$^{-1}$, 99 mAh g$^{-1}$, and 30 mAh g$^{-1}$ at the currents of 0.1 C, 0.2 C, 0.5 C, 1 C, 2 C, and 5 C, respectively. With the increase of ZIF-8 derived porous carbon particle size, the performance increases as the passage of multiple CNTs through the carbon particles ensures its good stability and high electronic/ionic conductivity. Conversely, because of the lack of the channels inside the big size of the ZIF-8 derived porous carbon particles, it is not

**Table 1. The cycle performance at 0.2 C and rate capacity of Se@ZIF-8-C and Se@ZIF-8-C@MWCNTs-X (X = 1-5)**

| Samples | Initial discharge capacity (mAh g$^{-1}$) | 2nd cycle discharge capacity (mAh g$^{-1}$) | 200th cycle discharge capacity (mAh g$^{-1}$) | Discharge capacity at 5 C (mAh g$^{-1}$) |
|---|---|---|---|---|
| Se@ZIF-8-C | 294 | 296 | 150 | 10 |
| Se@ZIF-8-C@MWCNTs-1 | 442 | 405 | 216 | 45 |
| Se@ZIF-8-C@MWCNTs-2 | 715 | 606 | 392 | 50 |
| Se@ZIF-8-C@MWCNTs-3 | 756 | 647 | 468 | 145 |
| Se@ZIF-8-C@MWCNTs-4 | 710 | 647 | 396 | 156 |
| Se@ZIF-8-C@MWCNTs-5 | 547 | 455 | 246 | 30 |

**Table 2. The rate capacity (mAh g$^{-1}$) at different current densities of Se@ZIF-8-C and Se@ZIF-8-C@MWCNTs-X (X = 1-5)**

| Samples | 0.1 C | 0.2 C | 0.5 C | 1 C | 2 C | 5 C |
|---|---|---|---|---|---|---|
| Se@ZIF-8-C | 220 | 180 | 100 | 40 | 20 | 10 |
| Se@ZIF-8-C@MWCNTs-1 | 250 | 192 | 150 | 100 | 60 | 45 |
| Se@ZIF-8-C@MWCNTs-2 | 600 | 520 | 405 | 284 | 143 | 50 |
| Se@ZIF-8-C@MWCNTs-3 | 675 | 584 | 496 | 391 | 260 | 145 |
| Se@ZIF-8-C@MWCNTs-4 | 660 | 582 | 517 | 426 | 306 | 156 |
| Se@ZIF-8-C@MWCNTs-5 | 564 | 467 | 343 | 205 | 99 | 30 |

beneficial to the ions transfer, leading to the electrochemical reaction kinetics drop. Thus, the optimal size of ZIF-8 derived carbon porous material at 300-500 nm achieves the best performance in the Li-Se battery. The cycling performance of Se@ZIF-8-C and Se@ZIF-8-C@MWCNTs-3 at a high current density of 1 C was conducted, as shown in Figure 5H. The capacity of Se@ZIF-8-C@MWCNTs-3 reaches 206 mAh g$^{-1}$ after 500 cycles, which is much higher than that of Se@ZIF-8-C at only 95 mAh g$^{-1}$. Therefore, the advantages of the composites of optimized ZIF-8-C size combined with the interconnected MWCNTs are fully demonstrated when compared with Se@ZIF-8-C at the high current density with a long cycle operation.

Figure 6A-C schematically illustrates the mechanism of electrochemical performances of Se@ZIF-8-C, ZIF-8-C@MWCNTs-1, and Se@ZIF-8-C@MWCNTs-5. The combination of ZIF-8 derived microporous carbon particles with highly conductive MWCNTs is beneficial for fast electron transportation in the electrode. It is observed that the particle size has a huge influence on the final electrochemical performances due to the following dilemmas: (A) the soluble polyselenides can easily escape from the micropores of ZIF-8-C if the particle size is too small; and (B) the selenium is not easily fully utilized inside micropores of ZIF-8-C if the particle size is too large. There exists a balance, where the suitable size of ZIF-8-C helps to achieve the best battery performance.

The EIS analysis was carried out at open circuit potential, and the results are shown in Figure 6D and E. For the fresh battery, the curves are composed of a semicircle at high frequency followed by a straight line at low frequency. The start point of the semicircle is R$_s$, which is assigned to the ohmic resistance of the coin cells[58], while the semicircle in the EIS is related to interface resistance between electrode and electrolyte, which is also called charge transfer impedance (R$_{ct}$)[59]. The relevant equivalent circuit model is inserted in the image. The chi-square values ($\chi^2$) between calculated result and measured data is within 10$^{-4}$. The
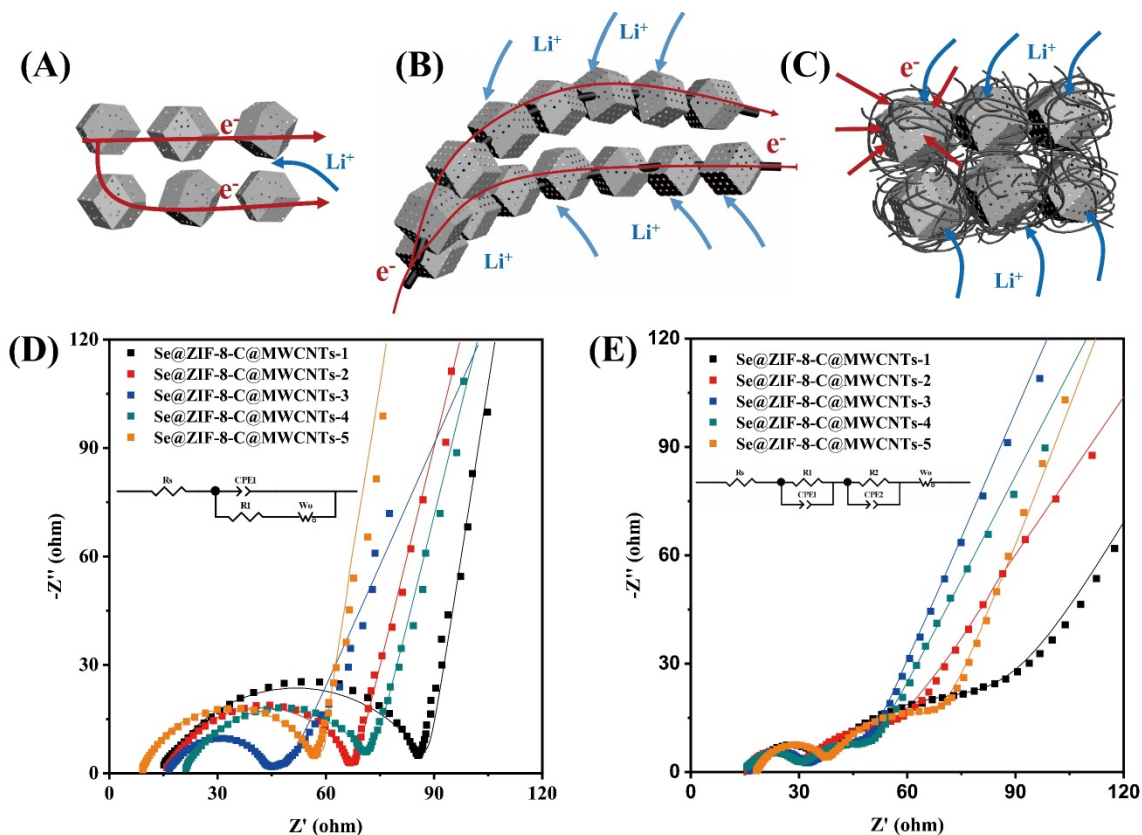
**Figure 6.** Schematic mechanism of the electrodes for lithium ion and electron movement: (A) Se@ZIF-8-C; (B) ZIF-8-C@MWCNTs-1; and (C) Se@ZIF-8-C@MWCNTs-5. Nyquist plots of Se@ZIF-8-C@MWCNTs-X (X = 1-5) electrode measured when fresh (D) and after 100 cycles with 0.2 C (E).

interface resistance has a huge influence on lithium ion and electron transportation. The interface resistance of Se@ZIF-8-C@MWCNTs-3 is 27 Ω, being much lower than all other electrodes. The clear second semicircle appears at the 100th cycle for the generation of the SEI layer[60]. The interface resistance ($R_{SEI}$) of Se@ZIF-8-C@MWCNTs-3 shows a similar tendency that proves the structural stability of the electrode. With the increase of ZIF-8 particle size, more carbon nanotubes pass through it, which improves the electrons transfer. However, a too big particle size of ZIF-8 is not beneficial to the transfer of ions. Thus, at the middle size of ZIF-8, Se@ZIF-8-C@MWCNTs-3 achieves the best reaction kinetics.

To better illustrate the relationship between ZIF-8 derived porous carbon particle size and the battery performance, the specific discharge capacity and impedance of the Se@ZIF-8-C@MWCNTs-X (X = 1-5) positive electrodes as a function of the particle size of the internal ZIF-8 derived porous carbon are summarized in Figure 7. With the increase of ZIF-8 derived porous carbon particle size, the number of CNTs that pass through the particles increases. That is favorable for the tight connection of particles with MWCNTs in the composites and rapid electronic conductivity of the positive electrode, leading to the improved capacity and stability of the battery. With the further increase of the ZIF-8 derived porous carbon particle size, the electrolyte and ion transfer are inhibited because of the increased depth of the micropores in the center of the particles, resulting in decrease in the capacity. Thus, the battery achieves the best performance when the ZIF-8 derived porous carbon particle and MWCNTs have an optimal combination. The optimal particle size of ZIF-8 derived porous carbon material at 300 nm-500 nm achieves the best performance in the Li-Se battery owing to the optimal reaction kinetics. The lowest EIS value of Se@ZIF-8-
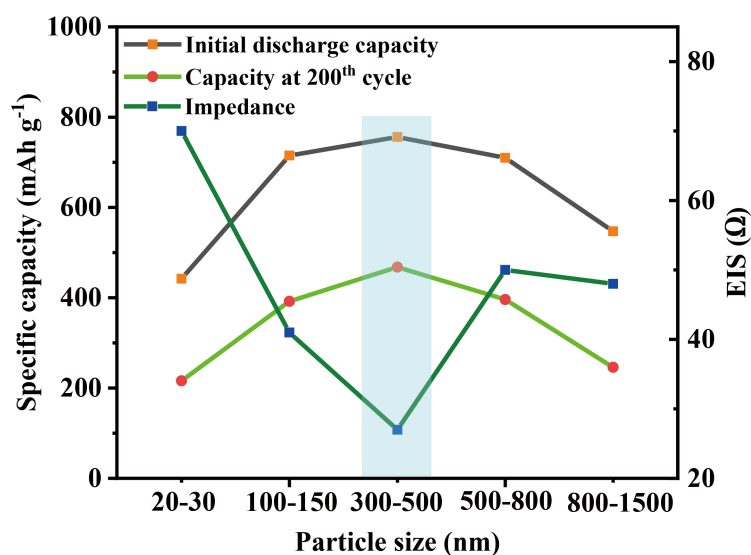
**Figure 7.** Summary of the specific capacity and impedance of the Se@ZIF-8-C@MWCNTs-X (X = 1-5) positive electrodes according to the particle size of the internal ZIF-8 derived porous carbon.

C@MWCNTs-3 from the impedance test again confirms the accelerated charge transfer.

## CONCLUSIONS

Series of microporous carbon particles derived from ZIF-8 strung by MWCNTs were obtained by in situ solvothermal reaction. The Se@ZIF-8-C@MWCNTs-X (X = 1-5) can benefit from the large microporosity of the ZIF-8 and much improved conductivity of MWCNTs for fast electron transportation. Besides, the interconnected 3D MWCNTs network formed fluffy structures can accelerate ions transfer and enhance adsorption of the polyselenides, which will further improve the electrochemical reaction and maintain the good stability of the battery. Importantly, the crystal size of ZIF-8 derived microporous carbon particles on the MWCNTs has a significant influence on the battery performance. The ZIF-8-C with particle size around 300-500 nm coated on MWCNTs, which gives Se@ZIF-8-C@MWCNTs-3 composite, possesses the highest conductivity and fast Li$^+$ transfer, thereby achieving the best performance with a capacity of 468 mAh g$^{-1}$ at 0.2 C after 200 cycles. The strategy developed in this work provides the facile way to obtain the connection of MOFs to MWCNTs to alleviate the inefficient electron transportation. The particle size of ZIF-8 derived microporous carbon should be thoroughly considered. In perspective, this strategy can be applied to the penetration of other MOFs by the conductive network to improve reaction kinetics for advanced Li-Se or Li-S batteries.

## DECLARATIONS

### Authors' contributions

Conceived the idea of the project: Su BL, Li Y

Made substantial contributions to conception and design of the study and performed data analysis and interpretation and wrote the draft of manuscript: Li HY, Li C

Performed data acquisition, as well as provided administrative, technical, and material support: Wang YY, Sun MH, Dong W

Discussed and revised the manuscript: Li Y, Su BL
Finalized the manuscript: Su BL

**Conflicts of interest**
All authors declared that there are no conflicts of interest.

**Ethical approval and consent to participate**
Not applicable.

**Consent for publication**
Not applicable.

## REFERENCES

1. Peng H, Huang J, Cheng X, Zhang Q. Lithium-sulfur batteries: review on high-loading and high-energy lithium-sulfur batteries (Adv. Energy Mater. 24/2017). *Adv Energy Mater* 2017;7:1770141.  DOI
2. Zhao M, Chen X, Li BQ, Li BQ, Huang JQ. An organodiselenide comediator to facilitate sulfur redox kinetics in lithium-sulfur batteries. *Adv Mater* 2021;33:e2007298.  DOI  PubMed
3. Zhang Y, Liu X, Wu L, et al. A flexible, hierarchically porous PANI/MnO$_2$ network with fast channels and an extraordinary chemical process for stable fast-charging lithium-sulfur batteries. *J Mater Chem A* 2020;8:2741-51.  DOI
4. Wang X, Tan Y, Liu Z, et al. New insight into the confinement effect of microporous carbon in Li/Se battery chemistry: a cathode with enhanced conductivity. *Small* 2020;16:e2000266.  DOI  PubMed
5. Lin S, Chen Y, Wang Y, et al. Three-dimensional ordered porous nanostructures for lithium-selenium battery cathodes that confer superior energy-storage performance. *ACS Appl Mater Interfaces* 2021;13:9955-64.  DOI  PubMed
6. Yang CP, Yin YX, Guo YG. Elemental selenium for electrochemical energy storage. *J Phys Chem Lett* 2015;6:256-66.  DOI  PubMed
7. Xiang H, Deng N, Zhao H, et al. A review on electronically conducting polymers for lithium-sulfur battery and lithium-selenium battery: progress and prospects. *Journal of Energy Chemistry* 2021;58:523-56.  DOI
8. Kim S, Cho M, Lee Y. High-performance Li-Se battery enabled via a one - piece cathode design. *Adv Energy Mater* 2019;10:1903477.  DOI
9. Jin J, Tian X, Srikanth N, Kong LB, Zhou K. Advances and challenges of nanostructured electrodes for Li-Se batteries. *J Mater Chem A* 2017;5:10110-26.  DOI
10. Li Z, Yuan L, Yi Z, Liu Y, Huang Y. Confined selenium within porous carbon nanospheres as cathode for advanced Li-Se batteries. *Nano Energy* 2014;9:229-36.  DOI
11. Zheng F, Yang Y, Chen Q. High lithium anodic performance of highly nitrogen-doped porous carbon prepared from a metal-organic framework. *Nat Commun* 2014;5:5261.  DOI  PubMed
12. Youn HC, Jeong JH, Roh KC, Kim KB. Graphene-selenium hybrid microballs as cathode materials for high-performance lithium-selenium secondary battery applications. *Sci Rep* 2016;6:30865.  DOI  PubMed  PMC
13. He J, Chen Y, Lv W, et al. Three-dimensional hierarchical graphene-CNT@Se: a highly efficient freestanding cathode for Li-Se batteries. *ACS Energy Lett* 2016;1:16-20.  DOI
14. Chen LH, Li Y, Su BL. Hierarchy in materials for maximized efficiency. *Natl Sci Rev* 2020;7:1626-30.  DOI  PubMed  PMC
15. Wu L, Li Y, Fu Z, Su BL. Hierarchically structured porous materials: synthesis strategies and applications in energy storage. *Natl Sci*

*Rev* 2020;7:1667-701.  DOI  PubMed  PMC

16.   Fan S, Zhang Y, Li S, Lan T, Xu J. Hollow selenium encapsulated into 3D graphene hydrogels for lithium-selenium batteries with high rate performance and cycling stability. *RSC Adv* 2017;7:21281-6.  DOI

17.   Fan JM, Chen JJ, Zhang Q, et al. An Amorphous carbon nitride composite derived from ZIF-8 as anode material for sodium-ion batteries. *ChemSusChem* 2015;8:1856-61.  DOI  PubMed

18.   Song JP, Wu L, Dong WD, et al. MOF-derived nitrogen-doped core-shell hierarchical porous carbon confining selenium for advanced lithium-selenium batteries. *Nanoscale* 2019;11:6970-81.  DOI  PubMed

19.   Yang CP, Xin S, Yin YX, Ye H, Zhang J, Guo YG. An advanced selenium-carbon cathode for rechargeable lithium-selenium batteries. *Angew Chem Int Ed Engl* 2013;52:8363-7.  DOI  PubMed

20.   Ji X, Lee KT, Nazar LF. A highly ordered nanostructured carbon-sulphur cathode for lithium-sulphur batteries. *Nat Mater* 2009;8:500-6.  DOI  PubMed

21.   Zhao Y, Song Z, Li X, et al. Metal organic frameworks for energy storage and conversion. *Energy Storage Materials* 2016;2:35-62.  DOI

22.   Wang L, Han Y, Feng X, Zhou J, Qi P, Wang B. Metal-organic frameworks for energy storage: Batteries and supercapacitors. *Coordination Chemistry Reviews* 2016;307:361-81.  DOI

23.   Liu X, Sun T, Hu J, Wang S. Composites of metal-organic frameworks and carbon-based materials: preparations, functionalities and applications. *J Mater Chem A* 2016;4:3584-616.  DOI

24.   Xu J, Lawson T, Fan H, Su D, Wang G. Updated metal compounds (MOFs, S, OH, N, C) used as cathode materials for lithium-sulfur batteries. *Adv Energy Mater* 2018;8:1702607.  DOI

25.   Pan Y, Liu Y, Zeng G, Zhao L, Lai Z. Rapid synthesis of zeolitic imidazolate framework-8 (ZIF-8) nanocrystals in an aqueous system. *Chem Commun (Camb)* 2011;47:2071-3.  DOI  PubMed

26.   Cravillon J, Münzer S, Lohmeier S, Feldhoff A, Huber K, Wiebcke M. Rapid room-temperature synthesis and characterization of nanocrystals of a prototypical zeolitic imidazolate framework. *Chem Mater* 2009;21:1410-2.  DOI

27.   Stolar T, Užarević K. Mechanochemistry: an efficient and versatile toolbox for synthesis, transformation, and functionalization of porous metal-organic frameworks. *CrystEngComm* 2020;22:4511-25.  DOI

28.   Zhou J, Li R, Fan X, et al. Rational design of a metal-organic framework host for sulfur storage in fast, long-cycle Li-S batteries. *Energy Environ Sci* 2014;7:2715.  DOI

29.   Tang J, Yamauchi Y. Carbon materials: MOF morphologies in control. *Nat Chem* 2016;8:638-9.  DOI  PubMed

30.   Dang S, Zhu Q, Xu Q. Nanomaterials derived from metal-organic frameworks. *Nat Rev Mater* 2018;3:17075.  DOI

31.   Lim S, Suh K, Kim Y, et al. Porous carbon materials with a controllable surface area synthesized from metal-organic frameworks. *Chem Commun (Camb)* 2012;48:7447-9.  DOI  PubMed

32.   Chaikittisilp W, Ariga K, Yamauchi Y. A new family of carbon materials: synthesis of MOF-derived nanoporous carbons and their promising applications. *J Mater Chem A* 2013;1:14-9.  DOI

33.   Wu HB, Lou XWD. Metal-organic frameworks and their derived materials for electrochemical energy storage and conversion: promises and challenges. *Sci Adv* 2017;3:eaap9252.  DOI  PubMed  PMC

34.   Liu Y, Si L, Zhou X, et al. A selenium-confined microporous carbon cathode for ultrastable lithium-selenium batteries. *J Mater Chem A* 2014;2:17735-9.  DOI

35.   Li X, Sun Q, Liu J, Xiao B, Li R, Sun X. Tunable porous structure of metal organic framework derived carbon and the application in lithium-sulfur batteries. *Journal of Power Sources* 2016;302:174-9.  DOI

36.   Kim D, Kim DW, Hong WG, Coskun A. Graphene/ZIF-8 composites with tunable hierarchical porosity and electrical conductivity. *J Mater Chem A* 2016;4:7710-7.  DOI

37.   Chen K, Sun Z, Fang R, Shi Y, Cheng H, Li F. Metal-organic frameworks (MOFs)-derived nitrogen-doped porous carbon anchored on graphene with multifunctional effects for lithium-sulfur batteries. *Adv Funct Mater* 2018;28:1707592.  DOI

38.   Park S, Park J, Kang YC. Selenium-infiltrated metal-organic framework-derived porous carbon nanofibers comprising interconnected bimodal pores for Li-Se batteries with high capacity and rate performance. *J Mater Chem A* 2018;6:1028-36.  DOI

39.   Yu W, Dong W, Li C, et al. Interwoven scaffolded porous titanium oxide nanocubes/carbon nanotubes framework for high-performance sodium-ion battery. *Journal of Energy Chemistry* 2021;59:38-46.  DOI

40.   Yuan L, Yuan H, Qiu X, Chen L, Zhu W. Improvement of cycle property of sulfur-coated multi-walled carbon nanotubes composite cathode for lithium/sulfur batteries. *Journal of Power Sources* 2009;189:1141-6.  DOI

41.   Lu C, Wang D, Zhao J, Han S, Chen W. A continuous carbon nitride polyhedron assembly for high-performance flexible supercapacitors. *Adv Funct Mater* 2017;27:1606219.  DOI

42.   Huang G, Zhang F, Du X, Qin Y, Yin D, Wang L. Metal organic frameworks route to in situ insertion of multiwalled carbon nanotubes in $Co_3O_4$ polyhedra as anode materials for lithium-ion batteries. *ACS Nano* 2015;9:1592-9.  DOI  PubMed

43.   Wu R, Wang DP, Rui X, et al. In-situ formation of hollow hybrids composed of cobalt sulfides embedded within porous carbon polyhedra/carbon nanotubes for high-performance lithium-ion batteries. *Adv Mater* 2015;27:3038-44.  DOI  PubMed

44.   Li C, Wang Y, Li H, et al. Weaving 3D highly conductive hierarchically interconnected nanoporous web by threading MOF crystals onto multi walled carbon nanotubes for high performance Li-Se battery. *Journal of Energy Chemistry* 2021;59:396-404.  DOI

45.   Mao Y, Li G, Guo Y, et al. Foldable interpenetrated metal-organic frameworks/carbon nanotubes thin film for lithium-sulfur batteries. *Nat Commun* 2017;8:14628.  DOI  PubMed  PMC

46.   Zhang H, Zhao W, Zou M, et al. 3D, mutually embedded MOF@Carbon nanotube hybrid networks for high-performance lithium-sulfur batteries. *Adv Energy Mater* 2018;8:1800013.  DOI

47.   Zhu J, Jiang Z. Electrochemical photocatalytic degradation of eriochrome black T dye using synthesized $TiO_2$@CNTs nanofibers. *Int J Electrochem Sci* 2021;16:210318.  DOI  PubMed

48.   Kulkarni G, Velhal N, Phadtare V, Puri V. Enhanced electromagnetic interference shielding effectiveness of chemical vapor deposited MWCNTs in X-band region. *J Mater Sci: Mater Electron* 2017;28:7212-20.  DOI

49.   Chen M, Lu Q, Li Y, Chu M, Cao X. ZnO@ZIF-8 core-shell heterostructures with improved photocatalytic activity. *CrystEngComm* 2021;23:4327-35.  DOI

50.   Dong W, Chen H, Xia F, et al. Selenium clusters in Zn-glutamate MOF derived nitrogen-doped hierarchically radial-structured microporous carbon for advanced rechargeable Na-Se batteries. *J Mater Chem A* 2018;6:22790-7.  DOI

51.   Balakumar K, Kalaiselvi N. Selenium containing tube-in-tube carbon: a one dimensional carbon frame work for selenium cathode in Li-Se battery. *Carbon* 2017;112:79-90.  DOI

52.   Liu T, Dai C, Jia M, et al. Selenium embedded in metal-organic framework derived hollow hierarchical porous carbon spheres for advanced lithium-selenium batteries. *ACS Appl Mater Interfaces* 2016;8:16063-70.  DOI  PubMed

53.   Dong W, Li C, Wang C, et al. Phase conversion accelerating "Zn-Escape" effect in ZnSe-CFs heterostructure for high performance Sodium-Ion half/full batteries. *Small*.  DOI

54.   Dong W, Wang D, Li X, et al. Bronze $TiO_2$ as a cathode host for lithium-sulfur batteries. *Journal of Energy Chemistry* 2020;48:259-66.  DOI

55.   Han K, Liu Z, Shen J, Lin Y, Dai F, Ye H. A free-standing and ultralong-life lithium-selenium battery cathode enabled by 3D mesoporous carbon/graphene hierarchical architecture. *Adv Funct Mater* 2015;25:455-63.  DOI

56.   Qiu R, Fei R, Zhang T, et al. Biomass-derived, 3D interconnected N-doped carbon foam as a host matrix for Li/Na/K-selenium batteries. *Electrochimica Acta* 2020;356:136832.  DOI

57.   Li H, Dong W, Li C, et al. Three-dimensional ordered hierarchically porous carbon materials for high performance Li-Se battery. *Journal of Energy Chemistry* 2022;68:624-36.  DOI

58.   Xiao L, Li E, Yi J, et al. Enhancing the performance of nanostructured ZnO as an anode material for lithium-ion batteries by polydopamine-derived carbon coating and confined crystallization. *Journal of Alloys and Compounds* 2018;764:545-54.  DOI

59.   Dong WD, Yu WB, Xia FJ, et al. Melamine-based polymer networks enabled N, O, S Co-doped defect-rich hierarchically porous carbon nanobelts for stable and long-cycle Li-ion and Li-Se batteries. *J Colloid Interface Sci* 2021;582:60-9.  DOI  PubMed

60.   Li Y, Dong B, Zerrin T, et al. State-of-health prediction for lithium-ion batteries via electrochemical impedance spectroscopy and artificial neural networks. *Energy Storage* 2020:2.  DOI

Bao-Lian Su created the Laboratory of Inorganic Materials Chemistry (CMI) at the University of Namur, Belgium in 1995. He is currently Full Professor of Chemistry, Member of the European Academy of Sciences, Member of the Royal Academy of Belgium, Fellow of the Royal of Society of Chemistry, UK and Life Member of Clare Hall College, University of Cambridge. He is also a strategy scientist at Wuhan University of Technology, China. He is the Editor-in-Chief of the *Chemical Synthesis*, Section Editor of the National Science Review and the Managing Editor of the NANO. His current research fields include the synthesis, the property study and the molecular engineering of organized, hierarchically porous and bio-organisms for artificial photosynthesis, (photo) Catalysis, Energy Conversion and Storage, Biotechnology, Cell therapy and Biomedical applications.

**Bao-Lian Su**

Yu Li received his B.S. from Xi'an Jiaotong University in 1999 and received his M.S. from Liaoning Shihua University in 2002. He obtained his Ph.D. from Zhejiang University in 2005. He worked in EMAT at the University of Antwerp with Prof. G. Vantendeloo in 2005 and then in CMI at the University of Namur with Prof. Bao-Lian Su in 2006. Currently, he is a full-time Professor at Wuhan University of Technology. His research interests include nanomaterials design and synthesis, hierarchically porous materials synthesis, and their applications in the fundamental aspects of energy and environment.

**Yu Li**

Hongyan Li received her ME degree in 2017 from Ocean University of China. She is a PhD candidate at the University of Namur, Inorganic Materials Chemistry (CMI). Her research interests mainly focus on Lithium-selenium battery, Lithium-ion battery and Dye-Sensitized Solar Cells.

**Hongyan Li**